15 Metabolic Bone Diseases and Drug-Induced Osteoporosis

Bone scintigraphy has traditionally been considered to be not as useful as radiography in the study of metabolic bone diseases including senile or postmenopausal osteoporosis, osteodystrophy, drug-induced osteoporosis, and rickets and osteomalacia. However, aided by the pinhole technique, ^{99m}Tc-MDP bone scintigraphy has been shown to be able to portray characteristic features in systemic and local osteoporosis or osteopenia, which is defined as a state of reduced bone mass with increased cavity. Rickets and osteomalacia, a state of deficient formation of inadequately mineralized osteoid, can also be efficiently diagnosed by bone scintigraphy. Indeed, it is well known that bone scintigraphy is highly sensitive and reliable for detecting fractures and infractions in porosis and Looser's zone (pseudofracture, osteoid seam) in osteomalacia, which often defy radiographic diagnosis when pathological changes are extensive. In addition and importantly, refined whole-body scintigraphy can uniquely demonstrate systemic involvement pattern of porosis and malacia. For example, whole-body scintigraphy shows generally decreased bone uptake in postmenopausal and senile osteoporosis (Fig. 15.1), increased tracer uptake in osteodystrophy of primary hyperparathyroidism with visualized kidneys (Fig. 15.2), increased tracer uptake in renal osteodystrophy without visualized kidneys (Fig. 15.3), and decreased tracer uptake in hepatic osteodystrophy (Fig. 15.4). Such valuable information can easily be extracted from a pair of anterior and posterior views, which are routinely obtainable at no additional expense.

Metabolic bone diseases result from a number of etiologies including endocrine disorders, renal and hepatic failure, disturbed calcium-phosphorus metabolism, vitamin C and D deficiency or D excess, and general undernourishment. The clinical entities of metabolic bone diseases are diverse, and symptoms and signs are complex. The present discussion is confined to (a) the involutional (senile and postmenopausal) osteoporosis, (b) disuse and immobilization osteoporosis, (c) osteodystrophy associated with primary and secondary hyperparathyroidism, (d) drug-induced osteoporosis, and (e) osteomalacia and rickets since these conditions are considered to be more common and can be easily approached diagnostically by radiography and scintigraphy. Regional osteoporosis related to hypervascularity and disuse has already been given full and partial accounts in the foregoing sections.

15.1 Involutional Osteoporosis

Involutional osteoporosis includes senile osteoporosis and postmenopausal osteoporosis. The reported incidences vary according to the diagnostic method used and the population studied. One radiographic study of spinal osteoporosis in a series of ambulatory women aged between 45 and 79 years recorded an incidence of 29% (Smith et al. 1960). Most recent studies have indicated a prevalence of 50% in women and 20% in men in their late seventies (Fujiwara 2004) and 11.4% in women of 50 years or older and 1.6% in men of the same age group (Yang et al. 2006).

Osteoporosis reflects the state of bone mass reduction that makes the bone brittle and fragile. Postmenopausal osteoporosis typically affects women in the sixth and seventh decades of life. In addition to reduced estrogen level, lowered physical activity and nutritional state are related to this condition. Histologically, involutional osteoporosis is characterized by a disproportionate reduction of the trabecular bone mass

Y.-W. Bahk, *Combined Scintigraphic and Radiographic Diagnosis of Bone and Joint Diseases*,
DOI 10.1007/978-981-10-2759-8_15

Fig. 15.1 Usefulness of whole-body bone scintigraphy in the study of systemic osteoporosis. Anterior (*left*) and posterior (*right*) whole-body scans in a 78-year-old woman with advanced osteoporosis show generally diminished skeletal uptake

compared to cortical bone mass, whereas senile osteoporosis shows a proportionate reduction of both the cortical and trabecular bone. The most common and problematic complication of involutional osteoporosis is the spinal and distal radial fractures. The femoral neck, proximal humerus, tibia, and pelvis are other common sites.

Radiographically, osteoporosis manifests as increased radiolucency and graying of bone which shows thin, sparse trabeculae and slim, deficient cortices. In the spine, the porotic vertebrae may present the characteristic “pencil-line contour” sign (Fig. 15.5a) and frequently the “fish vertebra”

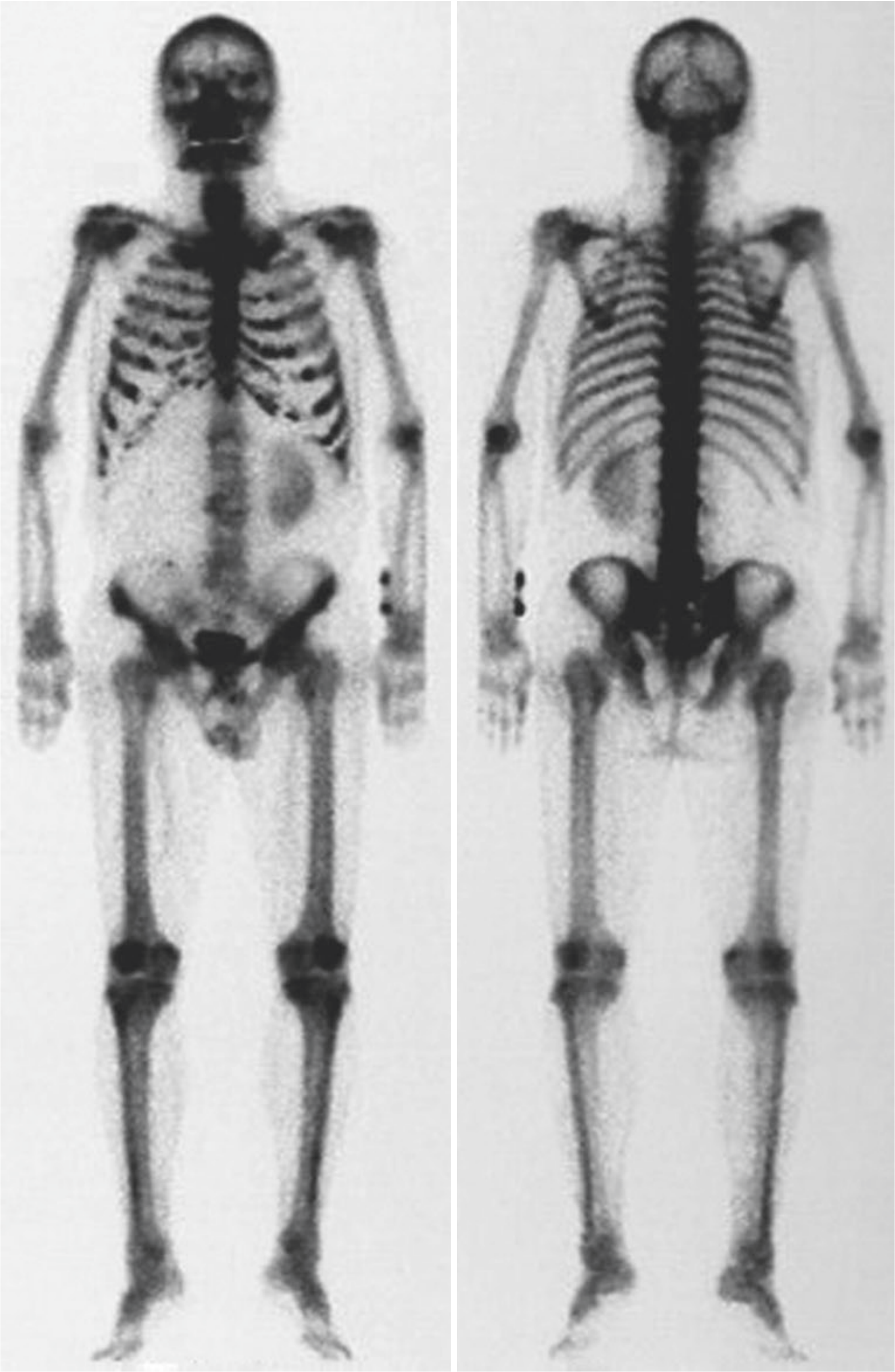

Fig. 15.2 Usefulness of whole-body bone scintigraphy in osteomalacia. Anterior (*left*) and posterior (*right*) whole-body scans in a 77-year-old man with primary hyperparathyroidism show generally increased skeletal uptake due to osteodystrophy with avaricious tracer uptake. Note the well-functioning left kidney

Fig. 15.3 Renal osteodystrophy. Anterior whole-body bone scintigraphy in a 73-year-old woman with end-stage renal failure and congestive heart failure shows generally increased tracer uptake with the most prominent uptake occurring in the skull. Note that both kidneys are not visualized and ribs are fractured (*arrows*)

deformity (Fig. 15.6a). Compression fracture with kyphosis is a hallmark of menopausal osteoporosis.

Scintigraphically, unlike markedly increased tracer uptake in transient osteoporosis, senile or postmenopausal osteoporosis is characterized by decreased uptake due to sharply reduced bone turnover (Fig. 15.1). Understandably, the subjective visual assessment of osteoporosis is inaccurate. More often than not, however, pinhole scintigraphy reveals the thinned cortices of long bones and vertebrae to be indistinct. This finding, arbitrarily termed the "pale bone" sign, reflects deficient tracer uptake in osteopenia (Fig. 15.5b). When a porotic vertebral endplate is fractured, tracer uptake becomes markedly intensified, distinctly standing out against the pale bones behind. The porotic lumbar vertebrae with either concave or biconcave endplates, the "fish vertebra" deformity, may also accumulate tracer, but the uptake is usually not so intense (Fig. 15.6b). Indeed, the intensity of tracer uptake in these two radiographically similar conditions clearly differs so that bone scintigraphy can discriminate one condition from the other. In general, fractures in the porotic bones and infractions (Looser's zone) in the malacic bones such as the spine and pelvis are extremely difficult to detect by radiographic examination, but such a problem can easily be solved with the use of bone scintigraphy (Figs. 15.4 and 15.7).

15.2 Disuse and Immobilization Osteoporosis

The bone is not a mere lazy weight-bearing or protective scaffold for the body, but is day and night engaged with modeling and remodeling through the active physicochemical and metabolic activities of osteoblasts and osteoclasts. Appropriate physical stress and strain are essential for maintaining such homeostatic functions in an orderly state. Thus, disuse and immobilization may result in mobilization of the calcium stored in the bone, leading to osteoporosis due to a negative balance with its level in the serum and urine sensitively changing. Osteoporosis may appear before 5–7 weeks in those under the age of 20 years and those over 50 years and more commonly after 8 weeks of immobilization (Jones 1969). The pathogenetic basis for decreased bone production and increased bone resorption has been debated, although Heaney (1962) demonstrated in a radiocalcium study that both bone resorption and formation are increased, but with more resorption than formation.

Radiographically, osteoporosis is characterized by graying of bone which has a washed-out appearance that is generalized, diffuse, regional, or local in occurrence (Fig. 15.8a) and its pattern is homogeneous, band-like, or streaky and speckled. The trabeculae are coarsened and the

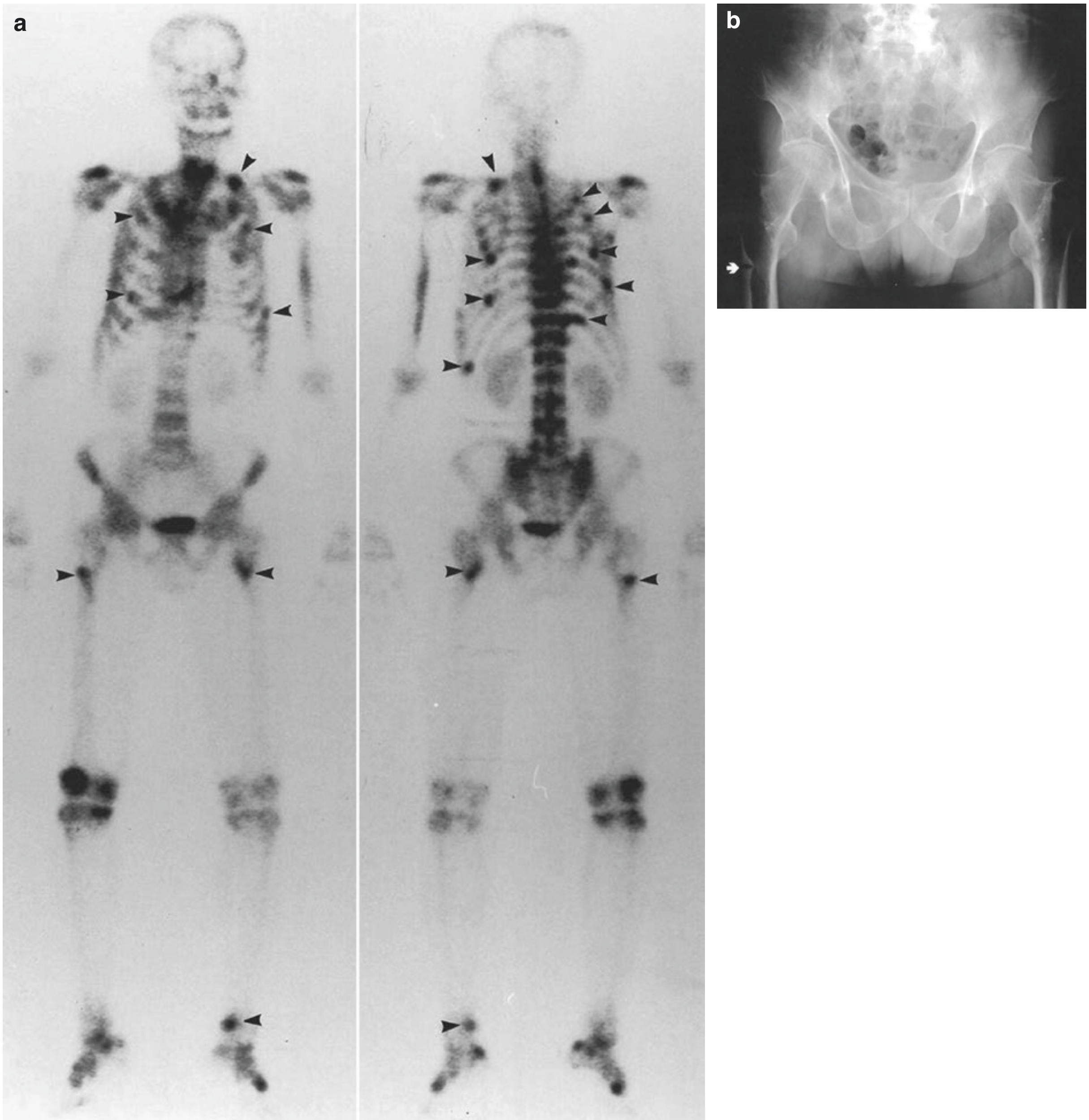

Fig. 15.4 Hepatic osteodystrophy with systemic osteoporosis. (**a**) Anterior (*left*) and posterior (*right*) whole-body bone scans in a 60-year-old man with alcoholic hepatopathy shows generalized low uptake with numerous bone infractions (*arrowheads*). (**b**) Anterior radiograph of the pelvis reveals a typical infraction in the lateral cortex of the right proximal femoral shaft (courtesy of Dr. H. Ohta, Department of Radiology, Osaka Medical School, Japan)

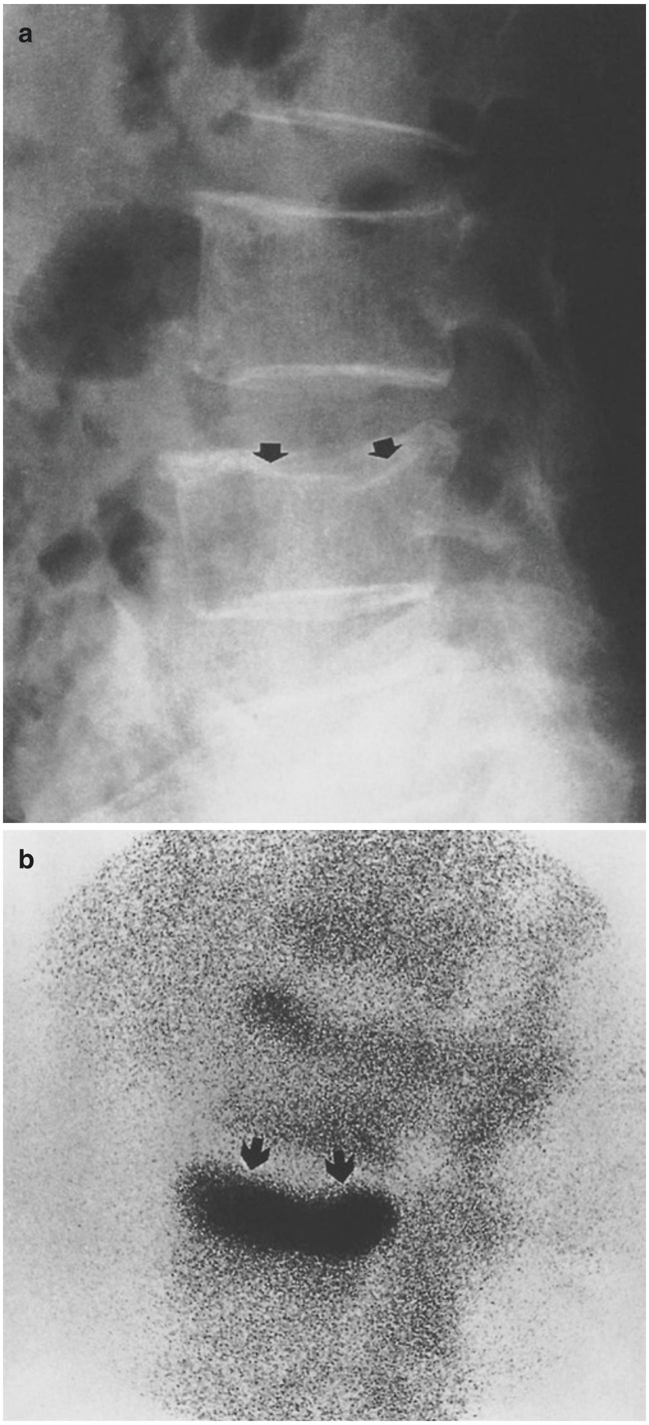

Fig. 15.5 Involutional osteoporosis. (**a**) Lateral radiograph of the midlumbar spine in a 55-year-old woman reveals generalized porosis and the classic "pencil-line" vertebral contour and compression fracture in the upper endplate of the L3 vertebra (*arrows*). (**b**) Lateral pinhole scintigraph portrays arcuate, intense tracer uptake in the upper endplate of the L3 vertebra (*arrows*). Observe the generalized low tracer uptake in the porotic spine, producing the "pale vertebra" sign

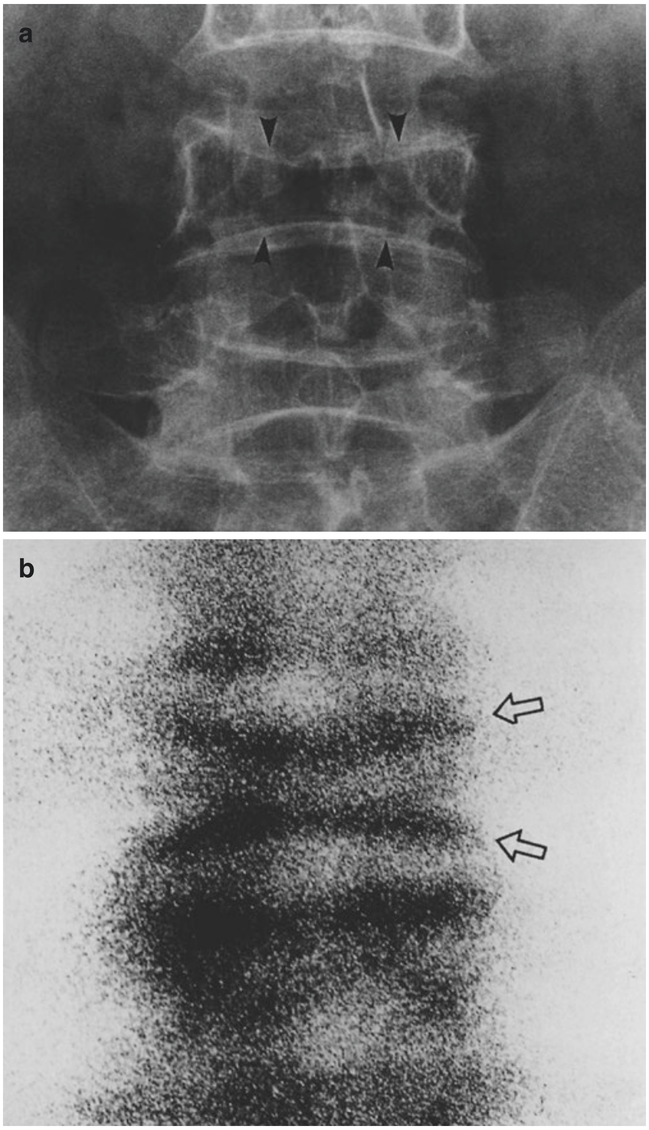

Fig. 15.6 Spinal osteoporosis with "fish vertebra" deformity and compression fracture. (**a**) Anteroposterior radiograph of the lower lumbar spine in a chronically bedridden 35-year-old woman shows generalized porosis and "fish vertebra" deformity in the L4 and L5 vertebrae (*arrowheads*). (**b**) Posterior pinhole scan of the midlumbar spine in another elderly woman with a similar porosis and "fish vertebra" deformity shows minimally increased tracer uptake in "fish vertebra" deformity of the L3 vertebra (*open arrows*)

cortex becomes pencil lined, lamellated, or scalloped (Fig. 15.9a).

Scintigraphic findings vary according to the duration, severity, extent, and type of osteoporosis and the age of the patient, and this diversity seems to reflect the varied nature of the pathogenesis. Generally, however, senile or

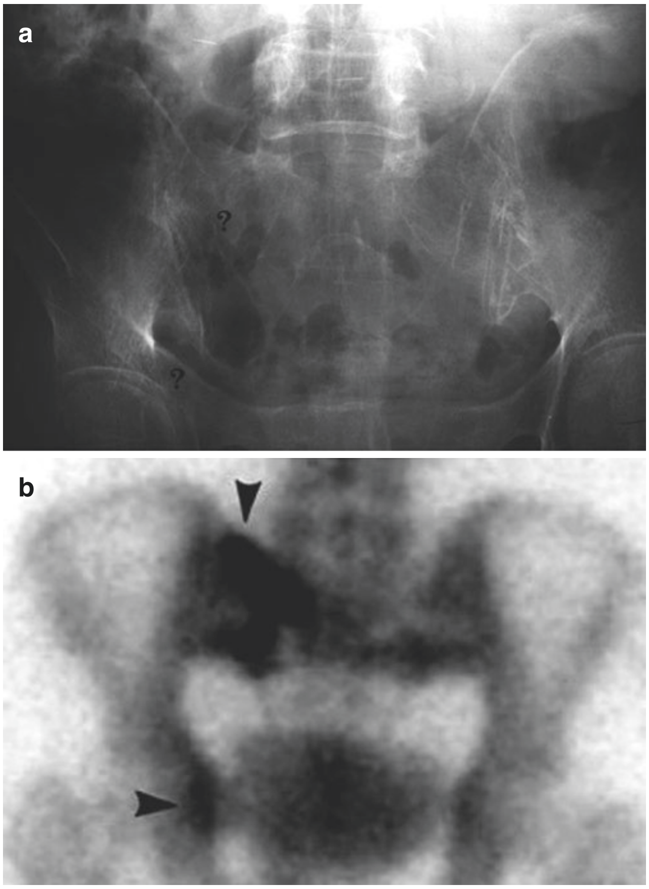

Fig. 15.7 Cryptic fractures in severe osteoporosis. (**a**) Anteroposterior radiograph of the pelvis in a 75-year-old woman with marked osteoporosis and fractures shows "blackening" of bones preventing the diagnosis of fractures (*?*). (**b**) Posterior bone scintigraph reveals low bone uptake due to porosis and two localized areas of intense uptake in the left sacroiliac joint and ischial tuberosity denoting fractures (*arrowheads*)

postmenopausal porosis (Fig. 15.1) and long-standing immobilization porosis (Fig. 15.9b) do not intensely accumulate tracer, and conversely, relatively acute and localized porosis observed in young and middle-aged patients shows prominent tracer uptake (Fig. 15.8b). The increased tracer uptake in regional or localized disuse porosis may slowly return to normal with active reuse (Fig. 15.10).

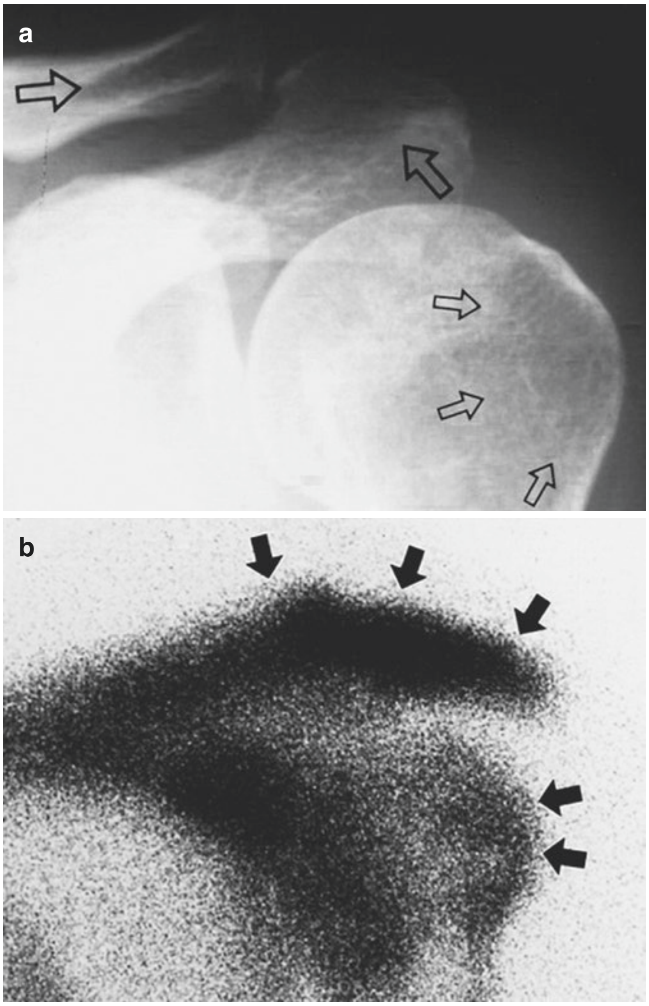

Fig. 15.8 Immobilization osteoporosis. (**a**) Anteroposterior radiograph of the left shoulder girdle in a 48-year-old woman with disuse after mastectomy for breast cancer shows diffusely "washed-out" regional bones (*open arrows*). (**b**) Anterior pinhole scintigraph reveals intense tracer uptake in porotic bones (*arrows*)

15.3 Osteodystrophy Associated with Hyperparathyroidism and Brown Tumor

Osteodystrophy associated with hyperparathyroidism is a well-established clinicopathological entity of radiographic and scintigraphic interest. Hyperparathyroidism may be classified into the primary, secondary, or tertiary form. The primary type results from increased parathormone production with resultant excessive bone calcium mobilization. The etiology includes adenoma (75%), hyperplasia, and carcinoma. This is a disease of middle age and older, and women are affected twice as frequently as men. The common clinical symptoms are primarily due to hypercalcemia, including weakness, lassitude, polydipsia, polyuria, renal stone, and constipation. The secondary form results from chronic renal or hepatic insufficiency and the tertiary form from long-standing secondary hyperparathyroidism with autonomous parathyroid function and hypercalcemia.

Radiographic changes basically consist of osteoporosis and osteomalacia with soft-tissue and vascular calcification,

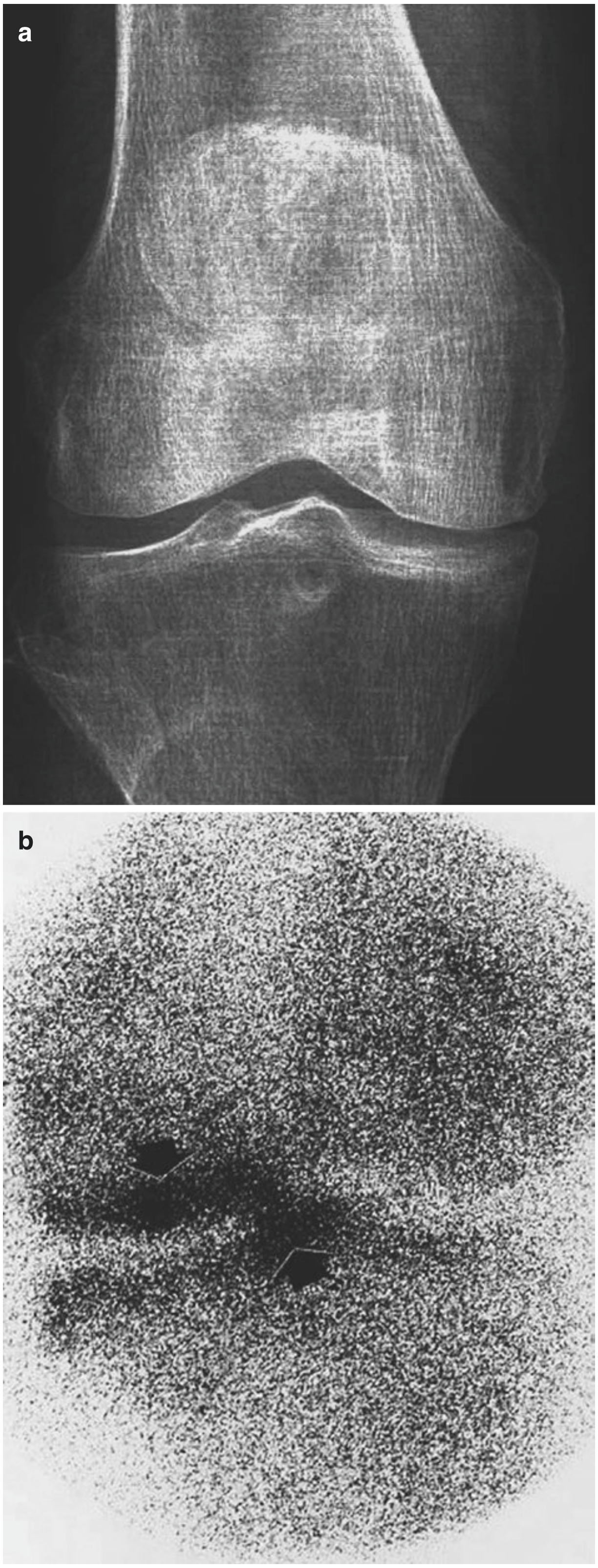

Fig. 15.9 Disuse osteoporosis. (**a**) Anteroposterior radiograph of the immobilized right knee in a 48-year-old woman due to osteoarthritis shows porosis with coarsened trabeculae and pencil-line cortex. No radiographic arthritic change is seen. (**b**) Anterior pinhole scintigraph reveals coarse speckled tracer uptake of porosis and zonal uptake of early osteoarthritis (*arrows*)

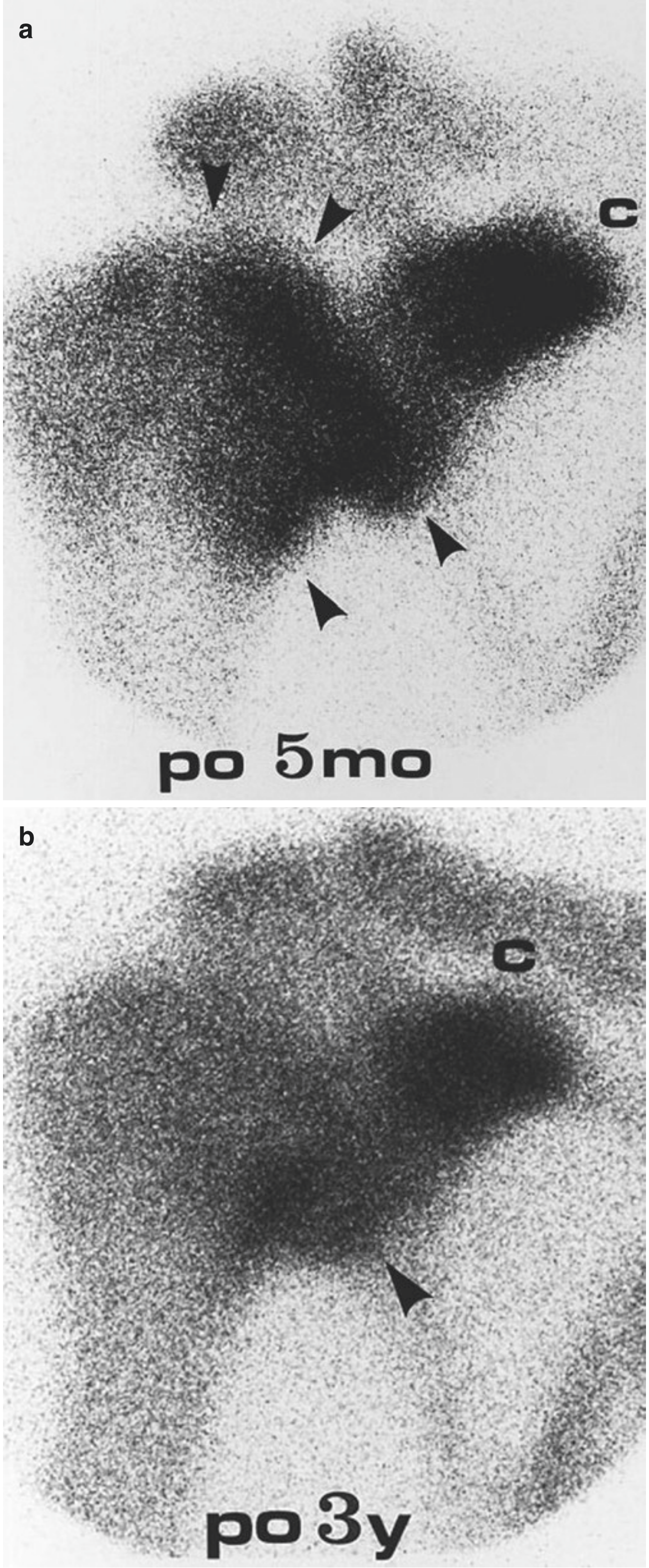

Fig. 15.10 Normal return of tracer uptake in disuse osteoporosis. (**a**) Initial anterior pinhole scintigraph of the right shoulder in a 48-year-old woman with local porosis caused by months of immobilization following ipsilateral mastectomy shows intense tracer uptake in the glenohumeral joint bones (*arrowheads*). (**b**) Follow-up scintigraph taken 3 years later reveals nearly normalized bone uptake (*arrowhead*) (*c* coracoid process)

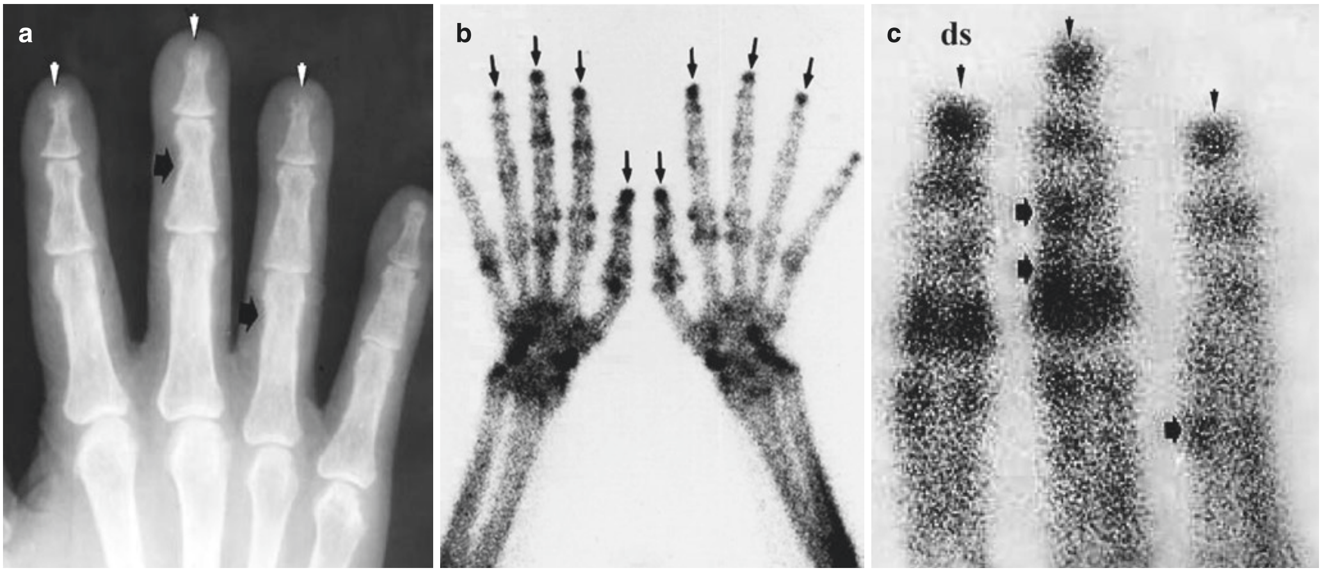

Fig. 15.11 Acrolysis and subperiosteal bone resorption in hyperparathyroidism. (**a**) Dorsopalmar radiograph of the right hand in a 56-year-old man with parathyroid adenoma shows generalized osteopenia with acrolysis (*top arrows*) and lacy subperiosteal bone resorption (*black arrows*). (**b**) Planar scan shows prominent tracer uptake in lysed tufts (*top arrows*) and diffuse granular uptake in the phalangeal and carpal bones. (**c**) Pinhole scan shows "drumstick-like" (*ds*) tracer uptake in the tufts (*top arrows*) and mottled uptake in the subperiosteal bone resorption (*arrows*)

manifesting as systemic demineralization, peculiar bone resorption, brown tumor, arterial calcification, and chondrocalcinosis. Bone resorption occurs in the subperiosteums, cortices, endosteums, and trabeculae and underneath the articular cartilages and ligaments. Of these, subperiosteal bone resorption with a lacelike change in the long bone is pathognomonic. Osteopenia, quantitatively assessed using bone densitometry, may widely vary in grade according to the severity and duration of the illness. Mild to moderate osteopenia in the early stage is difficult to diagnose by radiography, but advanced osteopenia manifests as a generalized decrease in bone mineral density with ground-glass-like change and the "salt-and-pepper" sign in the cranium. Subperiosteal bone resorption occurs most typically in the radial aspect of the phalangeal shafts as well as the tufts (Fig. 15.11a) and the tibia. Intracortical bone resorption creates small ovoid or cigar-shaped lucencies. Subchondral bone resorption may occur in the sacroiliac joints, symphysis pubis, diskovertebral joints, acromioclavicular joints, sternoclavicular joints, and glenohumeral joints (Fig. 15.12a). Another important feature is subligamentous bone resorption in the trochanters, ischial and humeral tuberosities, and coracoclavicular ligamentous insertion (Fig. 15.13a).

Brown tumors may occur both in primary and secondary hyperparathyroidism. Histologically, the tumors consist of osteoclasts, fibrosis, and giant cells and are prone to involve the facial bones, ribs, femora, and pelvic bones. We have documented a case of multiple brown tumors in a patient on chronic hemodialysis with renal osteodystrophy. The cystic tumors were seen in the proximal femur and inferior ischial ramus (Gomez et al. 2003) (Fig. 15.14a). The loss of the lamina dura is also an important finding, although not specific.

Scintigraphically, the intensity of tracer uptake in primary hyperparathyroidism appears to correlate with the severity of radiographic bone change, ranging from apparently normal to intense uptake. High-resolution scintigraphy may reveal the drumstick sign in the acrolysis of the fingers (Fig. 15.11b) and plaque-like uptake in subperiosteal bone resorption, typically in the radial aspect of the phalangeal shafts (Fig. 15.11c); these two findings are pathognomonic of hyperparathyroidism osteodystrophy. The calvaria, mandible, sternum, and shoulder bones show increased uptake (Sy 1974) (Fig. 15.12b, c). Another important change is subligamentous bone resorption indicated by tracer accumulation, for example, in the undersurface of the lateral part of the clavicle and the tip of the coracoid process, which are the insertion sites of the coracoclavicular ligament (Fig. 15.13b). Brown tumors show increased tracer uptake, the intensity of which appears to vary according to the type of tumor: the radiographically lucent cystic type accumulates tracer less intensely than the partially mineralized one does (Fig. 15.14b). On the other hand, the lateral scan of the skull reveals diffusely increased tracer uptake in the vertex, the

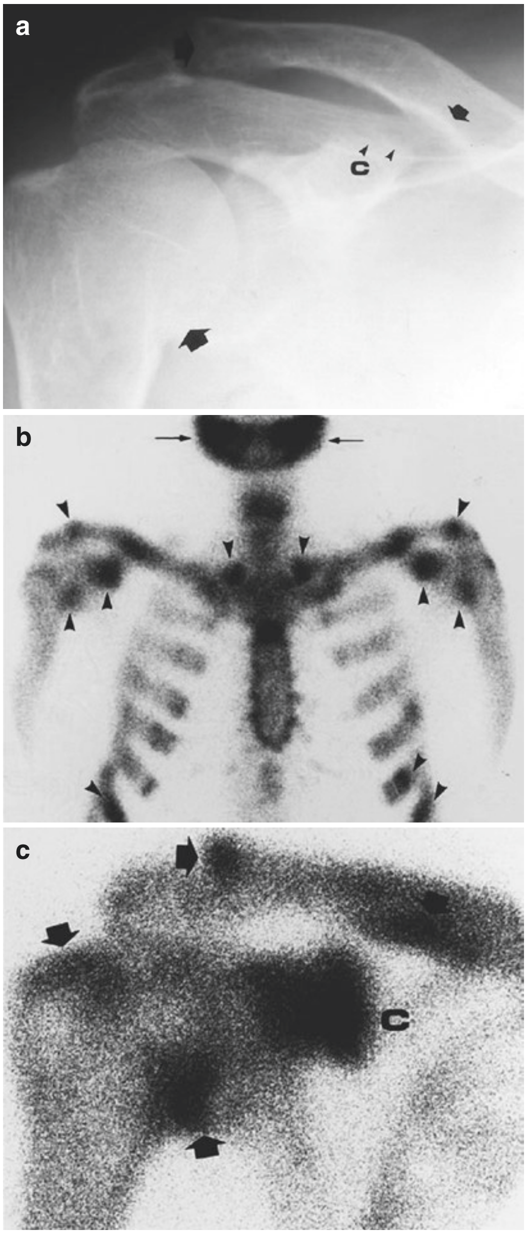

Fig. 15.12 Subchondral and subligamental bone resorption in hyperparathyroidism. (**a**) Anteroposterior radiograph of the right shoulder girdle in a 50-year-old man with primary hyperparathyroidism shows areas of subchondral bone resorptions in the acromioclavicular joint (*upper arrow*), medial glenohumeral joint (*lower arrow*), and coracoclavicular ligament (*c*). (**b**) Anterior planar scintigraph reveals areas of increased tracer uptake in the mandible, clavicles, coracoid processes, glenohumeral joints, and ribs bilaterally (*arrowheads*). The "hot" areas in the lower ribs represent infraction. (**c**) Anterior pinhole scintigraph shows tracer uptake in the lateral clavicular end, conoid ligament attachment (*upper arrow*), greater tuberosity, glenohumeral joint (*lower arrow*), and coracoid process (*c*)

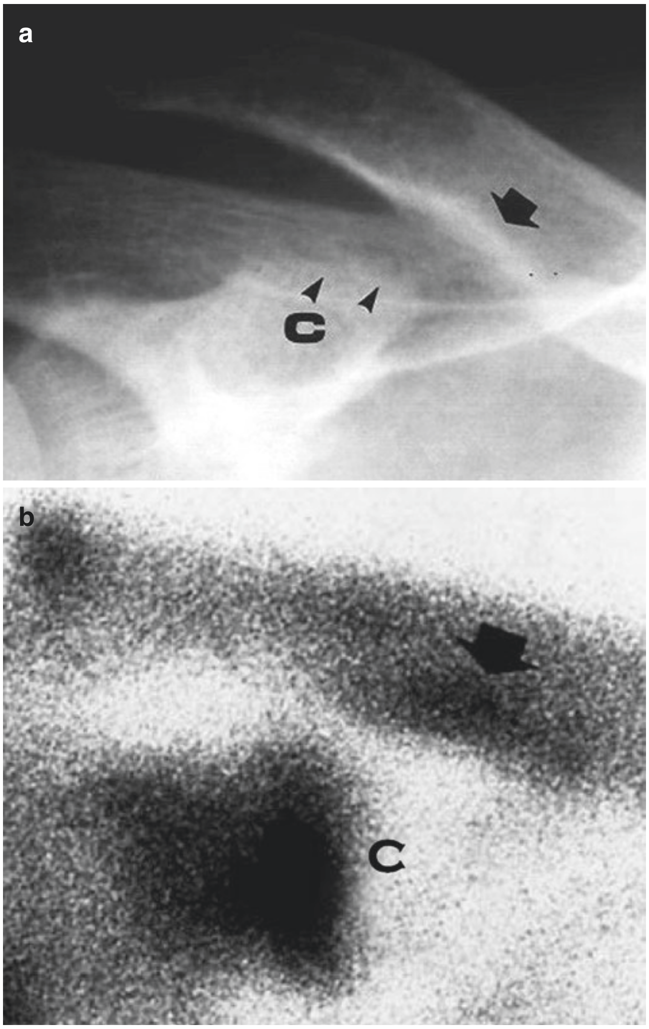

Fig. 15.13 Typical subligamental bone resorption in hyperparathyroidism. (**a**) Closeup radiograph of the right coracoconoid ligament attachments in Fig. 13.12 shows areas of subligamental bone resorption at the conoid tubercle (*arrow*) and the coracoid process (*c*). (**b**) Closeup pinhole scintigraph reveals well-defined areas of conspicuous tracer uptake at the conoid tubercle (*arrow*) and the coracoid process (*c*)

floor of the frontal bone, and the occipital bone (Fig. 15.15). Of interest, the magnified gamma correction pinhole scan showed that such uptake to consist of granular, pinpoint, and speckled components reflecting bone resorption and calcium mobilization. The finding appears to be the scintigraphic mirror image of the well-known radiographic "salt-and-pepper" sign.

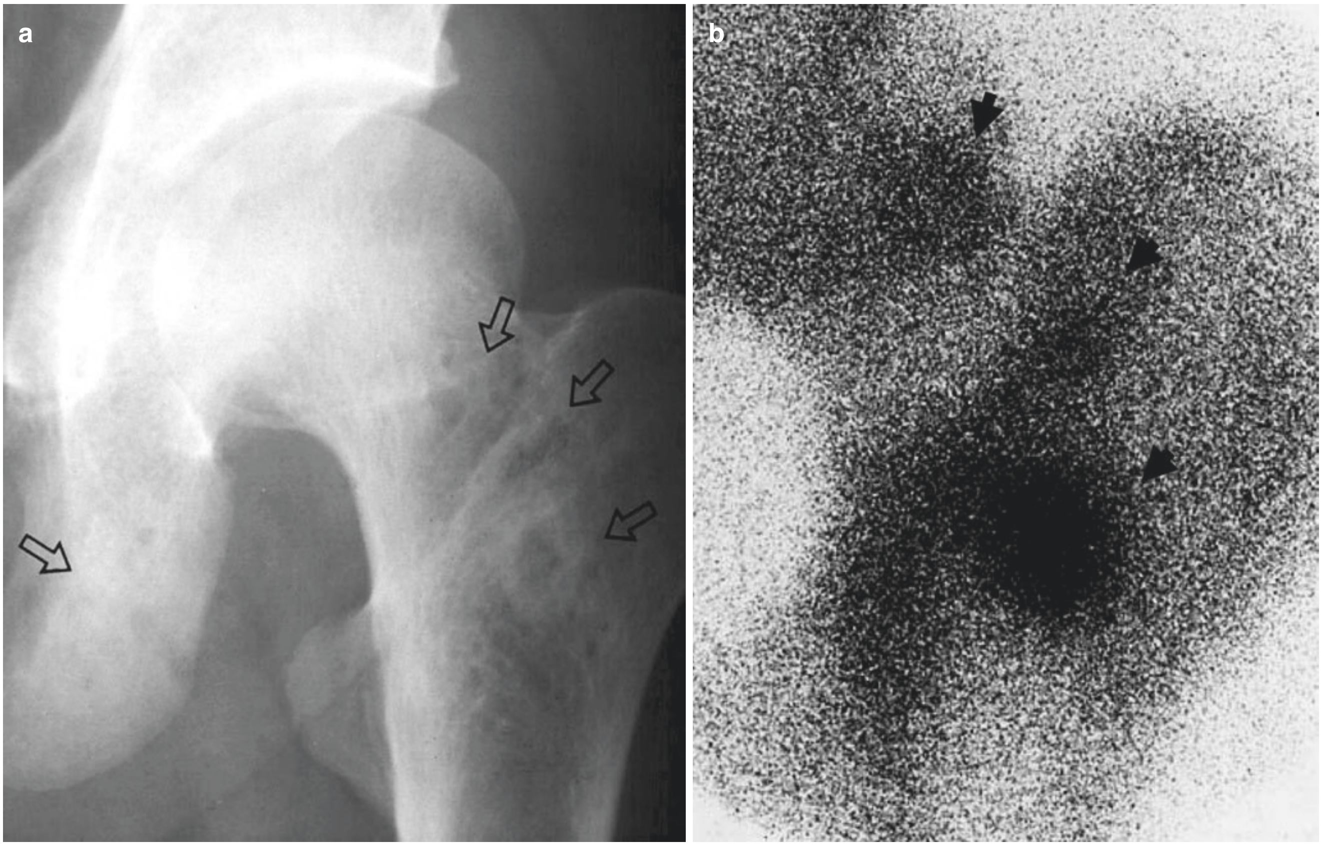

Fig. 15.14 Combined cystic brown tumors and sclerosis in hyperparathyroidism. (**a**) Anteroposterior radiograph of the left hip in a 49-year-old woman with hyperparathyroidism secondary to chronic renal failure shows multiple cystic brown tumors (*right open arrows*) and sclerosis (*left open arrow*). (**b**) Anterior pinhole scintigraph reveals multiple areas of intense uptake (*arrows*)

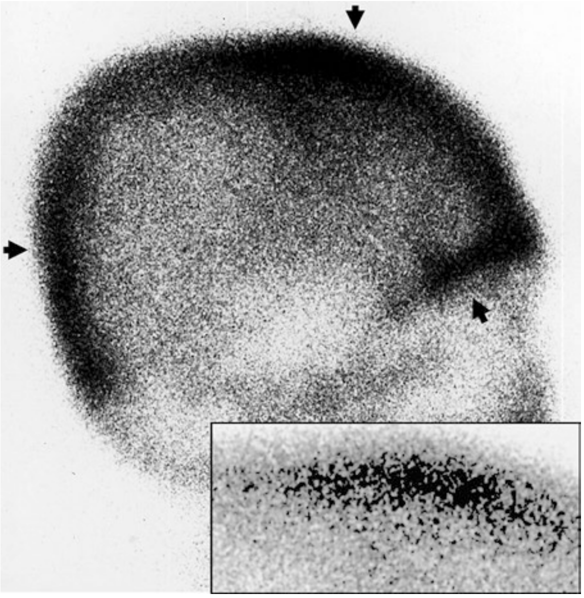

Fig. 15.15 Scintigraphic manifestation of the "salt-and-pepper" sign of the skull in hyperparathyroidism. Lateral pinhole scintigraph of the skull of the same patient as in Fig. 15.11 shows diffuse pinpoint and speckled uptake advantageously depicted on gamma correction scan (*inset*)

15.4 Drug-Induced Osteoporosis

Steroids, heparin, and methotrexate are well-known osteoporosis-inducing drugs. Of these, steroids cause osteoporosis by decreasing bone formation through the inhibition of osteoblast formation and by increasing bone resorption through either direct stimulation of osteoclasts or increasing parathormone release (Sambrook and Jones 1995). The hypercortisonism of Cushing's disease (endogenous and exogenous) also causes systemic osteoporosis. The daily administration of heparin in doses larger than 15,000 units has been reported to lead to osteoporosis in patients with myocardial infarction, thrombophlebitis, pulmonary emboli, or cerebral thrombosis (Griffith et al. 1965). A pathological study of biopsied bone from heparin-induced osteoporosis by Megard et al. (1982) demonstrated severe osteoporosis with rarefied spongy bone and increased osteoclasts and decreased osteoblasts. Unfractionated heparin causes symptomatic spinal fractures in up to 3% of patients on long-term treatment and osteopenia in 30% (Hawkins and Evans 2005). In addition, these authors reported that low-molecular-weight heparin reduces the risk of osteoporosis and spinal

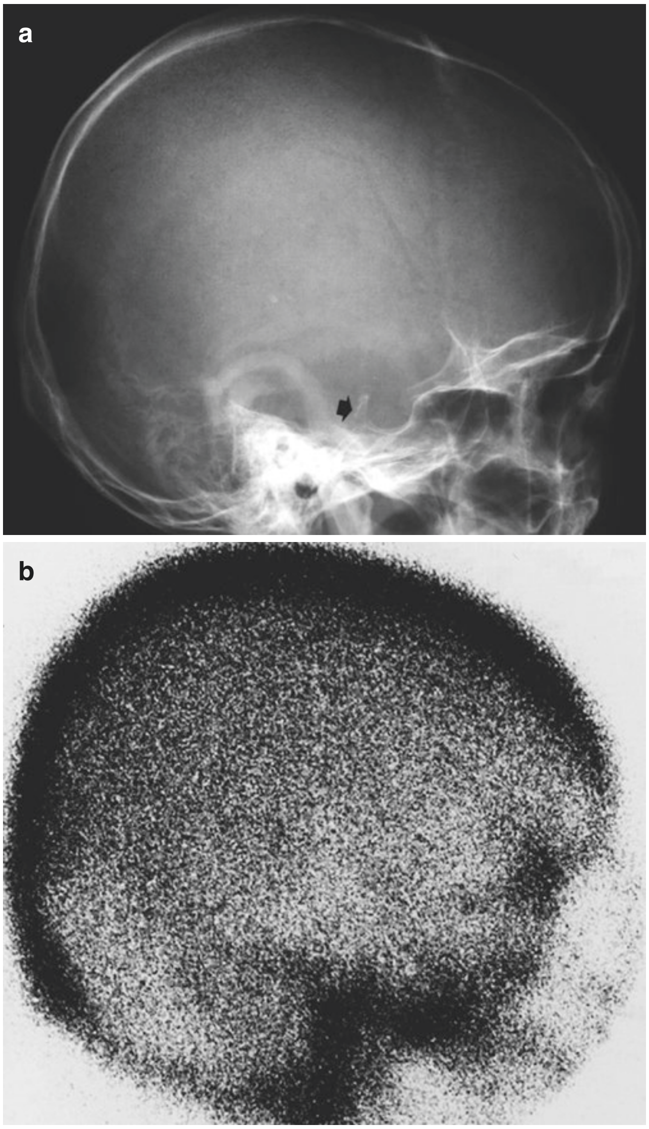

Fig. 15.16 Methotrexate-induced osteoporosis. (**a**) Lateral radiograph of the skull in a 50-year-old woman postoperatively treated with methotrexate for breast cancer shows diffuse porosis with white pencil-line cranial tables and washed-out sella (*arrow*). (**b**) Lateral pinhole scintigraph reveals diffusely increased tracer accumulation in the cranium and skull base with the salt-and-pepper sign

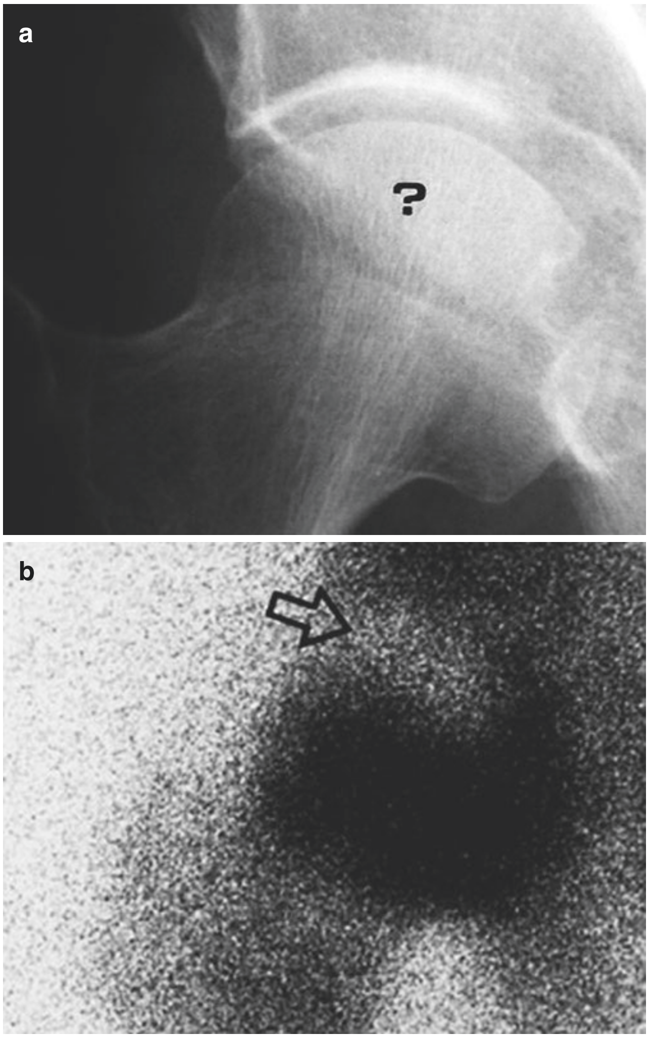

Fig. 15.17 Steroid-induced porosis and avascular osteonecrosis. (**a**) Anteroposterior radiograph of the right hip in a 62-year-old man treated with steroids for Wegener's granuloma of the nose shows no abnormality (*?*). (**b**) Anterior pinhole scintigraph reveals intense tracer uptake in the femoral head with an ovoid photon defect denoting avascular necrosis (*open arrow*)

fractures. Methotrexate is another medicine that may lead to iatrogenic osteoporosis (Mazanec and Grisanti 1989). It is used for the therapy of a wide variety of diseases including breast carcinoma, acute lymphocytic leukemia in children (Schwartz and Leonidas 1984), rheumatoid arthritis (Maenaut et al. 1997), systemic lupus erythematosus, psoriasis, and scleroderma (Singwe et al. 1998).

Radiographic changes of drug-induced osteoporosis are not dissimilar to those of osteoporosis of other etiologies. Thus, the fundamental feature is generalized graying of cancellous bones with cortical accentuation. The skull presents the pencil-line sign of the thinned outer and inner tables with graying of the squamosal portions (Fig. 15.16a). The hip is one of the most common sites of steroid-induced osteoporosis and avascular osteonecrosis, showing coarsened trabeculae (Fig. 15.17a). Insufficiency fractures of the spine and sacrum and infractions of the ribs are other important features. Frequently, fractures and infractions are not detected because of profound osteopenia. Calluses in insufficiency fractures tend to be extensive, clearly standing out against gray bones in the background.

Scintigraphic features include a generalized increase in bone uptake, especially in young patients, with more intense tracer uptake in fractures and infractions. In the skull, drug-induced osteoporosis is indicated by markedly increased uptake in the entire cranial vault seen tangentially and by coarse granular uptake in the squamosal portion seen en face (Fig. 15.16b). Bone scanning is extremely useful for detecting avascular necrosis, which often accompanies steroid-induced osteoporosis (Fig. 15.17b). Osteonecrosis is painful, but may often pass undetected by radiography in the early stages (Fig. 15.17a). Exogenous Cushing's disease manifests as increased tracer uptake in the skull, facial bones, ribs, spine, and pelvis as well as arthropathy for which steroids are prescribed (Kingsley and Hickling 1986) (Fig. 15.18).

15.5 Rickets and Osteomalacia

As mentioned above, rickets and osteomalacia are due to deficient formation of inadequately mineralized osteoid. The basic difference between the two closely related conditions is that the former occurs in actively growing bones and the latter in mature bones. Etiological factors include deficiency of vitamin D and its active hormonal form 1,25-dihydroxyvitamin D3 and disturbed calcium-phosphorus metabolism. The functions of the vitamin D series include the homeostatic maintenance of calcium and phosphorus as well as bone mineralization. The active from of vitamin D acts on the intestine and bone as well as the kidneys and parathyroid glands. In the intestine, it helps absorb calcium and phosphorus and in the bone it mediates mobilization and redeposition of both ions. Hence, malabsorption syndromes, chronic renal failure with secondary hyperparathyroidism, and renal tubular disorder with acidosis may create osteomalacia.

Radiographically, rickets is characterized by, in addition to graying and a washed-out appearance of the entire skeleton, the absence of the provisional calcification zones, widening and blurring of the physes, fraying and cupping of the metaphyses, and dwarfed deossified ossification centers (Fig. 15.19a). Osteomalacia also manifests as diffuse graying of bones with a washed-out appearance because of poor mineralization. While rickets typically involves the long-bone ends and costochondral junctions in children, osteomalacia is characterized by Umbauzone or infractions in the stressed sites of the scapula, lower rib cage, pubic rami, and proximal femora in adults (Fig. 15.20).

Bone scintigraphic manifestations of rickets and osteomalacia can be divided into systemic and regional. For the observation of systemic changes, a whole-body image is suitable and for the visualization of the individual lesions, pinhole scintigraphy is ideal. Whole-body scintigraphy shows increased tracer uptake in the entire skeleton, making it sharply contrasted with the background (Fig. 15.18b).

Fig. 15.18 Exogenous Cushing's disease. Posterior whole-body bone scintigraphy in a 68-year-old woman under long-term treatment with steroids for rheumatoid arthritis shows tracer uptake in the skull, facial bones, ribs, spine, and pelvis (*arrows*) as well as polyarthritis (*arrowheads*)

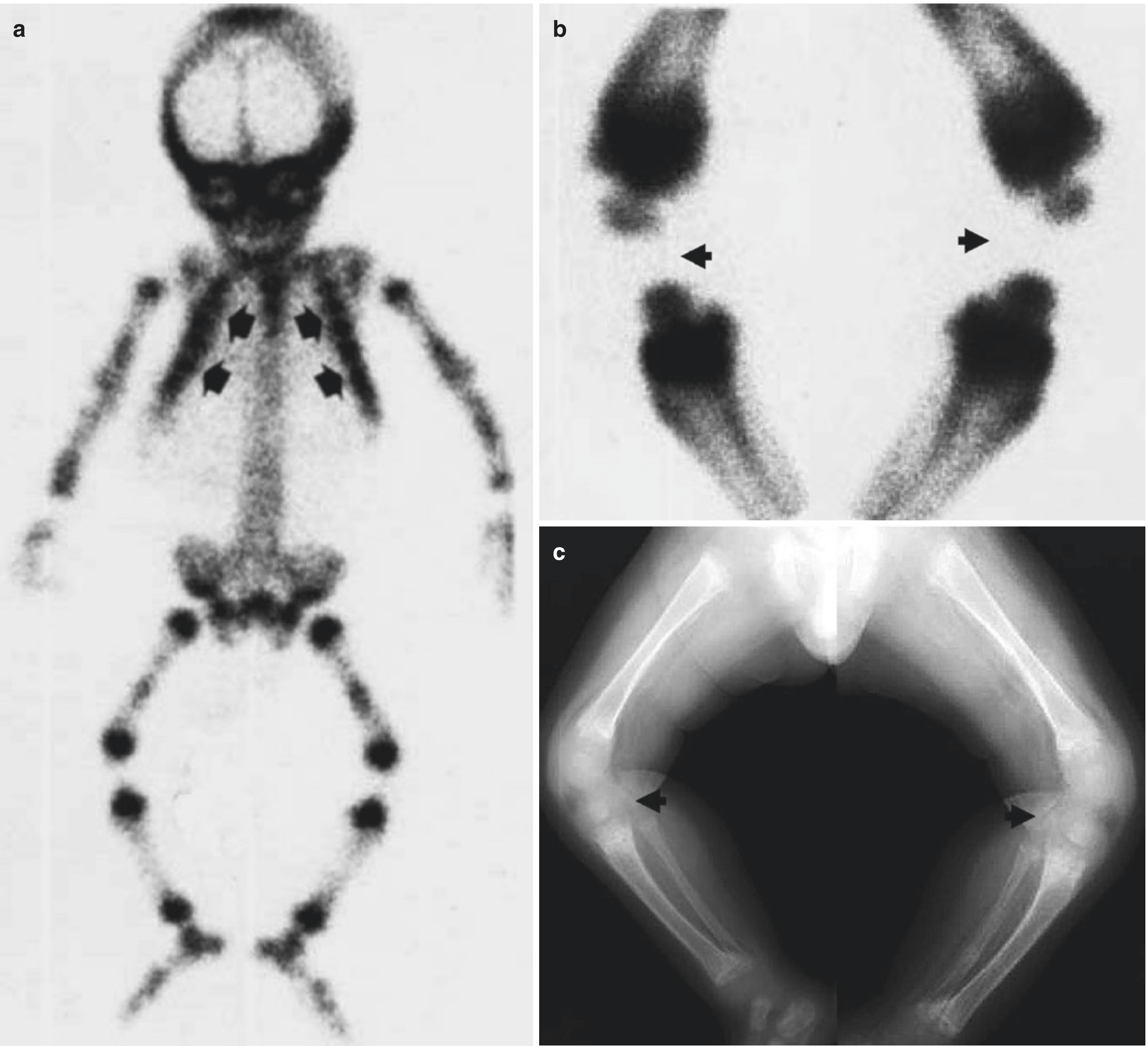

Fig. 15.19 Rickets. (**a**) Whole-body scan in a 12-month-old male baby with advanced rickets shows the spectrum of skeletal changes including "superscan" and "rosary" sign of beaded costochondral junctions (*arrows*). (**b**) Pinhole scans of the knees show prominent tracer uptake in the flared metaphyses of the femora and tibiae with underdeveloped epiphyseal centers giving rise to a "chicken bone" appearance (*arrows*). Joint spaces appear widened. (**c**) Radiograph shows generalized deossification, vanished provisional ossification zones, wide physeal plates, and metaphyseal flaring (*arrows*)

Sy and Mittal (1975) called such a finding "superscan," and it is a sensitive indicator of altered bone metabolism. The kidneys show little or no tracer uptake because of renal dysfunction or drainage of available bone tracer by avaricious bones of malacia. This phenomenon occurs more typically in the osteomalacia of renal osteodystrophy (Fig. 15.3). Small spotty "hot" areas in the infractions in the peripheries of stressed bones such as the lower ribs (Fig. 15.12b) and the pubic bones and proximal femora with the "superscan" sign are pathognomonic (Fogelman et al. 1977) (Fig. 15.20). Pinhole scanning of rickets shows intense uptake in the flared metaphyses and dwarfed epiphyseal ossification cen-

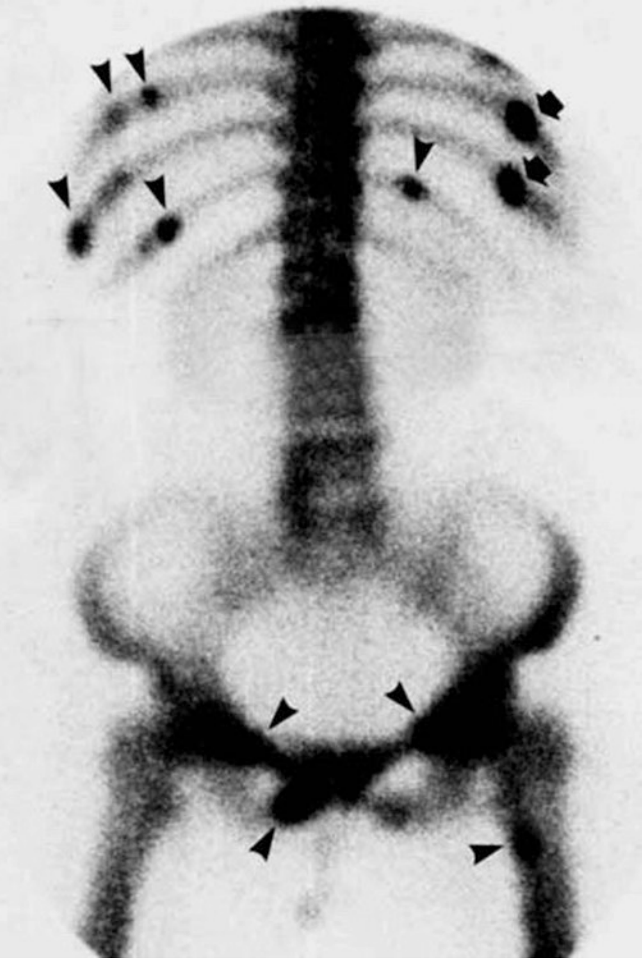

Fig. 15.20 Multiple hot spots of infractions and "superscan" in hyperparathyroidism. A composite scintigraph of the trunk (posterior view) and the pelvis (anterior view) in a 76-year-old woman with hyperparathyroidism shows multiple hot spots in the lower rib cage, the pelvic bones, and the left proximal femur (*arrowheads*). Typically, infractions are aligned vertically in the rib cage. The two larger hot spots in the right lower rib cage represent actual fractures (*arrows*)

ters of the long bones, producing the "chicken bone" sign (Fig. 15.19c). The articular spaces appear spuriously widened due to dystrophic ossification centers (epiphyses) and bulky cartilages. On the other hand, the osteomalacia of primary hyperparathyroidism (Fig. 15.2) and renal osteodystrophy (Fig. 15.3) manifests as increased tracer uptake in the axial skeleton including the calvaria, mandible, rib cage, and sternum.

Other scintigraphic findings of osteodystrophy include the "tie sternum" sign, the "striped tie" sign, and costochondral beading or the "rosary" sign (Fig. 15.19b). The "hot patella" sign is not specific, occurring in many diverse conditions such as chondromalacia patellae, metastasis, and disuse porosis (Fogelman et al. 1983; Bahk et al. 1994). Pinhole scintigraphy is very useful for studying and archiving increased bone turnover focally in infraction or diffusely in the malacic skeleton. Its use is encouraged for the study of subtle subperiosteal bone resorption (Fig. 15.11), subchondral bone resorption (Fig. 15.12c), subtendinous bone resorption (Fig. 15.13b), and brown tumors or cystic change (Fig. 15.14b).

15.6 Diabetic Neuroarthropathy

Diabetic neuroarthropathy and peripheral arterial disease of systemic atherosclerosis are two leading causes of pedal bone destructive disease. Disabling and often mutilating such disease is not only a challenge for medicine and podiatry but also the imaging sciences. About 25% of diabetics are assumed to develop one or other type of foot disease in their lifetime (Giurato and Uccioli 2006). Clinically, diabetic neuroarthropathy may be complicated by septic arthritis, osteomyelitis, osteolysis, ulceration, and gangrene. The association of diabetes with other osteoarthropathies such as gouty arthritis, rheumatoid arthritis, and Forestier's ankylosing hyperostosis are generally regarded as coincidental.

Conventional radiography is useful for anatomical diagnosis of diabetic foot (Tomas et al. 2000). Radiographic features are protean, including articular sclerosis, narrowing, and destruction, osteopenia, osteolysis, subluxation, deformity, and bone atrophy (Fig. 15.21a). With the refinement of technique, CT angiography and MR angiography are now competitively used for the diagnosis of peripheral arterial disease (Gardner and Afaq 2008), and MR imaging in neuropathic arthropathy can even detect sinus tract, soft-tissue fat change, and bone marrow alteration as complications (Ahmadi et al. 2006). Scintigraphically, conventional ^{67}Ga citrate scan and ^{111}In leucokyte scan are used for the diagnosis of bone infection in diabetes (Palestro and Love 2007). It has been shown that the combined use of ^{99m}Tc-HDP angiography and magnified planar equilibrium scanning performed in one sitting can enrich the diagnostic contents and enhance the diagnostic acumen in diabetic neuroarthropathy. Indeed, nuclear angiography reliably reveals decreased or absent blood flow in ischemia and increased blood flow and blood pool in infected phalanges, and equilibrium bone scan presents photopenia in ischemia or gangrene (Fig. 15.21c). On occasion, scintiangiography can diagnose ischemia before radiographic change takes place (Fig.15.22a, b), and the

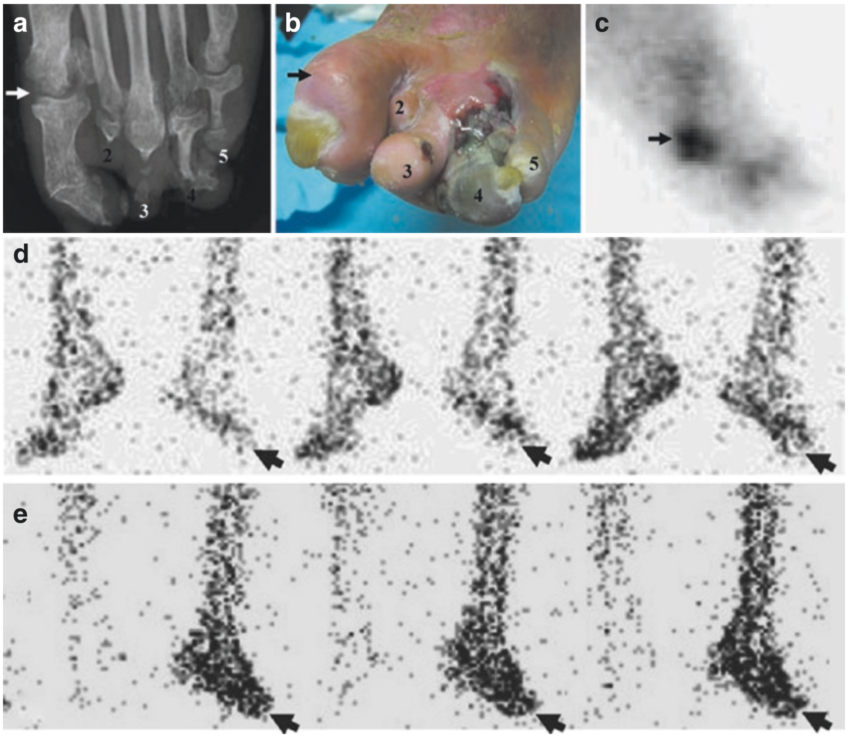

Fig. 15.21 Protean changes of chronic infective diabetic neuroarthropathy and assessment of vasodilator effect. (**a**) Dorsoplantar radiograph of the left forefoot in a 63-year-old man shows fragmentation, subluxation, and flexion of the first toe (*arrow*), atrophy, pointing, narrowing, and bending of other phalanges, amputation of the second toe, scar atrophy of the third toe, and gangrene in the fourth and fifth toes. (**b**) Photograph shows swelling of the first toe (*arrow*), the absence of the second toe, scar contraction of the third toe, and gangrene of the fourth and fifth toes. (**c**) Planar scan uniquely shows an infective focus with high uptake in the first metatarsophalangeal joint (*arrow*). (**d**) Initial scintiangiograph shows ischemia in the left foot (*arrow*). (**e**) Follow-up after vasodilator therapy for 3 months shows improved blood flow (*arrow*)

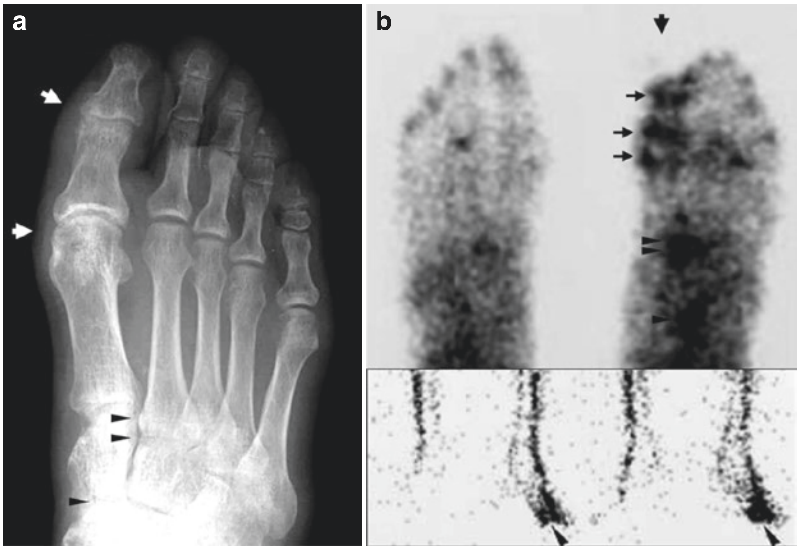

Fig. 15.22 Pre-radiographic diagnosis of diabetic neuroarthropathy using triple bone scan. (**a**) Dorsoplantar radiograph of the right foot in a 57-year-old male diabetic with recurrent inflammation in the first toe shows diffuse swelling of the soft tissue in the metatarsophalangeal and interphalangeal joints (*arrows*) without bony change. Infective arthritis is seen in the first-second intercuneiform joint (*paired arrowhead*). (**b**) Equilibrium planar scan shows photon defect in the distal phalanx (*top arrow*) and irregular bone uptake in the infective interphalangeal joints (*small arrows*). Infection is indicated by high uptake in the first-second intercuneiform joint (*paired arrowhead*) and the naviculocuneiform joints (*arrowhead*). Scintiangiograph shows regional increased blood flow and blood pool with vascular defect in the first toe (*arrowhead*)

Fig. 15.23 Neuroarthropathy with resection of the first toe. (**a**) Dorsoplantar radiograph in a 64-year-old female diabetic with gangrenous acrolysis of the left second toe tip and early osteolysis in the middle phalanx shows the absence of the distal phalanx (*top arrow*) and trabecular effacement in the middle phalanx (*bottom arrow*). Magnified view in inset shows the changes in detail. (**b**) Dorsal planar scan shows photopenia in the second toe tip (*top arrow*) and increased uptake in the melting middle phalanx (*bottom arrow*). Scintiangiograph shows vascular occlusion and hyperemia in the second toe (*arrow*)

equilibrium bone scan may demonstrate the signs of septic arthritis and osteomyelitis (Figs. 15.22b and 15.23b). Early osteolysis is indicated by increased tracer uptake (Fig.15.23a, b). It is worthy of mention that nuclear angiography is a noninvasive, economical, and useful means to first diagnose ischemia and gangrene and then assess and archive improved circulation in diabetic foot after the administration of vasodilator drug (Agarwal et al. 2005) (Fig. 15.21d, e).

References

Agarwal P, Agarwal PK, Sharma D, Baghel KD (2005) Intravenous infusion for the treatment of diabetic and ischemic non-healing pedal ulcers. J Eur Acad Dermatol Venereol 19:158–162

Ahmadi ME, Morrison WB, Carrino JA et al (2006) Neuropathic arthropathy of the foot with and without superimposed osteomyelitis: MR imaging characteristics. Radiology 238:622–631

Bahk YW, Park YH, Chung SK, Kim SH, Shinn KS (1994) Pinhole scintigraphic sign of chondromalacia patellae in older subjects: a prospective assessment with differential diagnosis. J Nucl Med 35:855–862

Fogelman I, McKillop JH, Greig WR et al (1977) Pseudo-fracture of the ribs detected by bone scanning. J Nucl Med 18:1236–1237

Fogelman I, McKillop JH, Gray HW (1983) The “hot patella” sign: is it of any clinical significance? J Nucl Med 24:312–315

Fujiwara S (2004) Epidemiology of osteoporosis and fracture (in Japanese). Clin Calcium 14:13–18

Gardner AW, Afaq A (2008) Management of lower extremity peripheral arterial disease. J Cardiopulm Rehabil Prev 28:349–357

Giurato L, Uccioli L (2006) The diabetic foot: Charcot joint and osteomyelitis. Nucl Med Commun 27:745–749

Gomez MC, Riquelme P, Sirandoni G et al (2003) Brown tumors in multiple locations: manifestation of severe renal osteodystrophy. Case report (in Spanish). Rev Med Chil 131:1183–1187

Griffith CC, Nichols G, Asher JD et al (1965) Heparin osteoporosis. JAMA 193:91–94

Hawkins D, Evans J (2005) Minimising the risk of heparin-induced osteoporosis during pregnancy. Expert Opin Drug Saf 4:583–590

Heaney RP (1962) Radiocalcium metabolism in disuse osteoporosis in man. Am J Med 33:188–200

Jones G (1969) Radiological appearance of disuse osteoporosis. Clin Radiol 20:249–253

Kingsley GH, Hickling P (1986) Polyarthropathy associated with Cushing's disease. Br Med J (Clin Res Ed) 292(6532):1363

Maenaut K, Westhovens R, Dequeker J (1997) Methotrexate osteopathy, does it exist? J Rheumatol 23:2156–2159

Mazanec DJ, Grisanti JM (1989) Drug-induced osteoporosis. Cleve Clin J Med 56:297–303

Megard M, Cuche M, Grapeloux A et al (1982) Heparin osteoporosis: histomorphometric analysis of bone biopsy. One case (in French). Nouv Press Med 11:261–264

Palestro CJ, Love C (2007) Radionuclide imaging of musculoskeletal infection: conventional agents. Semin Musculoskelet Radiol 11:335–352

Sambrook PN, Jones G (1995) Corticosteroid osteoporosis. Br J Rheumatol 34:8–12

Schwartz AM, Leonidas JC (1984) Methotrexate osteopathy. Skelet Radiol 11:13–16

Singwe N, De Gars L, Karneff A et al (1998) Multiple stress fractures in a scleroderma patient on methotrexate therapy. Rev Rheum Engl Ed 65:508–510

Smith RW Jr, Eyler WR, Mellinger RC (1960) On the incidence of senile osteoporosis. Ann Intern Med 25:855–862

Sy WM (1974) Bone scan in primary hyperparathyroidism. J Nucl Med 15:1089–1091

Sy WM, Mittal AK (1975) Bone scan in chronic dialysis patients with evidence of secondary hyperparathyroidism and renal osteodystrophy. Br J Radiol 48:878–884

Tomas MB, Patel M, Marwin SE, Palesrtro CJ (2000) The diabetic foot. Br J Radiol 73:443–450

Yang NP, Deng CY, Chou YJ et al (2006) Estimated prevalence of osteoporosis from a Nationwide Health Insurance database in Taiwan. Health Policy 75:329–337